

# Center to limb observations and modeling of the Ca I 4227 Å line

H. D. Supriya<sup>1</sup>, H. N. Smitha<sup>1</sup>, K. N. Nagendra<sup>1</sup>, J. O. Stenflo<sup>2,3</sup>, M. Bianda<sup>3</sup>, R. Ramelli<sup>3</sup>,  
B. Ravindra<sup>1</sup>, and L. S. Anusha<sup>4</sup>

<sup>1</sup>*Indian Institute of Astrophysics, Bangalore 560034, India*

<sup>2</sup>*Institute of Astronomy, ETH Zurich, CH-8093 Zurich, Switzerland*

<sup>3</sup>*Istituto Ricerche Solari Locarno, Via Patocchi, CH-6605 Locarno-Monti, Switzerland*

<sup>4</sup>*Max Planck Institut für Sonnensystemforschung, Justus-von-Liebig-Weg 3, D-37077 Göttingen, Germany*

hdsupriya@iiap.res.in; smithahn@iiap.res.in; knn@iiap.res.in; stenflo@astro.phys.ethz.ch;  
mbianda@irsol.ch; ramelli@irsol.ch; ravindra@iiap.res.in; bhasari@mps.mpg.de

## ABSTRACT

The observed center-to-limb variation (CLV) of the scattering polarization in different lines of the Second Solar Spectrum can be used to constrain the height variation of various atmospheric parameters, in particular the magnetic fields via the Hanle effect. Here we attempt to model non-magnetic CLV observations of the  $Q/I$  profiles of the Ca I 4227 Å line recorded with the ZIMPOL-3 at IRSOL. For modeling, we use the polarized radiative transfer with partial frequency redistribution with a number of realistic 1-D model atmospheres. We find that all the standard FAL model atmospheres, used by us, fail to simultaneously fit the observed  $(I, Q/I)$  at all the limb distances ( $\mu$ ). However, an attempt is made to find a single model which can provide a fit at least to the CLV of the observed  $Q/I$  instead of a simultaneous fit to the  $(I, Q/I)$  at all  $\mu$ . To this end we construct a new 1-D model by combining two of the standard models after modifying their temperature structures in the appropriate height ranges. This new combined model closely reproduces the observed  $Q/I$  at all the  $\mu$ , but fails to reproduce the observed rest intensity at different  $\mu$ . Hence we find that no single 1-D model atmosphere succeeds in providing a good representation of the real Sun. This failure of 1-D models does not however cause an impediment to the magnetic field diagnostic potential of the Ca I 4227 Å line. To demonstrate this we deduce the field strength at various  $\mu$  positions without invoking the use of radiative transfer.

*Subject headings:* line: formation – methods: numerical – polarization – radiative transfer – scattering – Sun: atmosphere

## 1. Introduction

Coherent scattering processes in the solar atmosphere causes the emitted radiation to be linearly polarized. The spectrum so obtained is referred to as the Second Solar Spectrum (SSS). This linearly polarized spectrum gets modified at the line core in the presence of weak magnetic fields due to the Hanle effect. One of the commonly observed and well studied lines in the SSS is the strong, chromospheric Ca I 4227 Å line (see for example, Stenflo et al. 1980; Stenflo 1982; Gandorfer 2002). This is a normal Zeeman triplet line arising

due to transition between the atomic states with total angular momentum  $J = 0 \rightarrow 1 \rightarrow 0$ . It exhibits largest scattering polarization among all lines in the Sun's visible spectrum (Stenflo et al. 1980). The core of the Ca I 4227 Å line is formed around a height of about 1000 km above the photosphere making it chromospheric in nature. The Hanle effect in the core of the Ca I 4227 Å line was first observed by Stenflo (1982).

One of the interesting feature exhibited by this line is the spatial variation of the wing polarization in  $(Q/I, U/I)$  spectra along the spectrograph slit. Bianda et al. (2003) noticed these variations

in the observations near an active region. Later these spatial variations were also observed in quiet regions by Sampoorana et al. (2009) and were interpreted to be arising due to the local inhomogeneities in the atmospheric layers. A detailed modeling of the Ca I 4227 Å line profile observed in a quiet region near the solar limb is presented by Anusha et al. (2010). The authors employed last scattering approximation to model them. Observations of the forward scattering Hanle effect in the Ca I 4227 Å line near the disk center were performed by Bianda et al. (2011). Subsequently these observations were modeled by Anusha et al. (2011) to determine the chromospheric weak magnetic fields.

One of the early attempts to model the polarization profiles of the Ca I 4227 Å line observed in both quiet and active regions was by Faurobert-Scholl (1992). The author used the observations of Stenflo (1982). Her treatment included the effects of partial frequency redistribution (PRD) and radiative transfer (RT).

To better understand the physics of scattering and to exploit it for various diagnostic purposes, we need to systematically study the center-to-limb variation (CLV) of the SSS. This will help us sample the height information of the atmospheric parameters and magnetic fields, as observations made at different lines of sight (LOS) sample different heights in the solar atmosphere. Few attempts have been made so far in detailed modeling of the CLV observations of ( $I$ ,  $Q/I$ ) spectra of atomic and molecular lines in the SSS. The most challenging aspect of such CLV modeling is to find a single model atmosphere which can fit both  $I$  and  $Q/I$  at all limb distances  $\mu$  ( $= \cos \theta$ ), simultaneously. One such attempt was made by Holzreuter & Stenflo (2007) to model CLV of the Ca II K line. They discuss the possibility of constructing a two-component atmospheric model (using a combination of a hot and a cool atmospheric component) to achieve a fit to the observed CLV profiles. A height dependent mixing ratio was required by them in order to simultaneously fit  $I$  and  $Q/I$  spectra at all the limb distances. They also demonstrate that a single atmospheric model with optimized temperature structure can be used to achieve a fit to the Ca II K line CLV data. However they find that different extents of modification in the temperature structure are re-

quired for different limb distances ( $\mu$ ). Another paper in which such CLV studies have been done is that of Shapiro et al. (2011) who consider the molecular CN violet system. They discuss the general problems involved in obtaining a simultaneous fit to the  $I$  and  $Q/I$  profiles using the standard 1-D single atmospheric model, as well as two-component atmospheric models. They finally construct an anisotropy modified single 1-D atmospheric model to simultaneously fit  $I$  and  $Q/I$  at all  $\mu$ .

The CLV of the Ca I 4227 Å line away from the active regions was first observed by Stenflo et al. (1980) and analyzed by Auer et al. (1980). The CLV of the line center polarization observed by Stenflo et al. (1980) was later used by Faurobert-Scholl (1994) to study the Hanle effect due to the magnetic field canopies in the chromosphere. The CLV observations of this line was also done by Bianda et al. (1998, 1999). In this paper we attempt a detailed simultaneous modeling of the observed CLV of both  $I$  and  $Q/I$  profiles of the Ca I 4227 Å line. For this purpose we solve the polarized RT equation by taking account of PRD effects in the non-magnetic regime. Standard 1-D atmospheric FAL models (Fontenla et al. 1993; Avrett 1995) are used to obtain a fit to the ( $I$ ,  $Q/I$ ) spectra. We find that it is not possible to achieve a simultaneous ( $I$ ,  $Q/I$ ) fit to the CLV observations with a single 1-D model atmosphere. If we consider the CLV of  $Q/I$  alone, then we find it necessary to modify the original temperature structure of the standard FAL atmospheric models to obtain a fit. Such modifications of the original temperature structure were also used in previous works by Holzreuter & Stenflo (2007); Smitha et al. (2012, 2013). In the present paper, the original temperature structure of the standard FAL-A atmosphere is modified. Later, the modified FAL-A ( $\overline{\text{FALA}}$ ) is combined with FAL-X atmospheric model to construct a single component model. It turns out that this newly constructed combined model can closely reproduce the observed  $Q/I$  at different limb distances.

In Section 2 we give the details of the CLV observations. Section 3 is devoted to the modeling procedure and the results. Section 4 describes the observational analysis to determine the magnetic fields. Concluding remarks are given in Section 5.

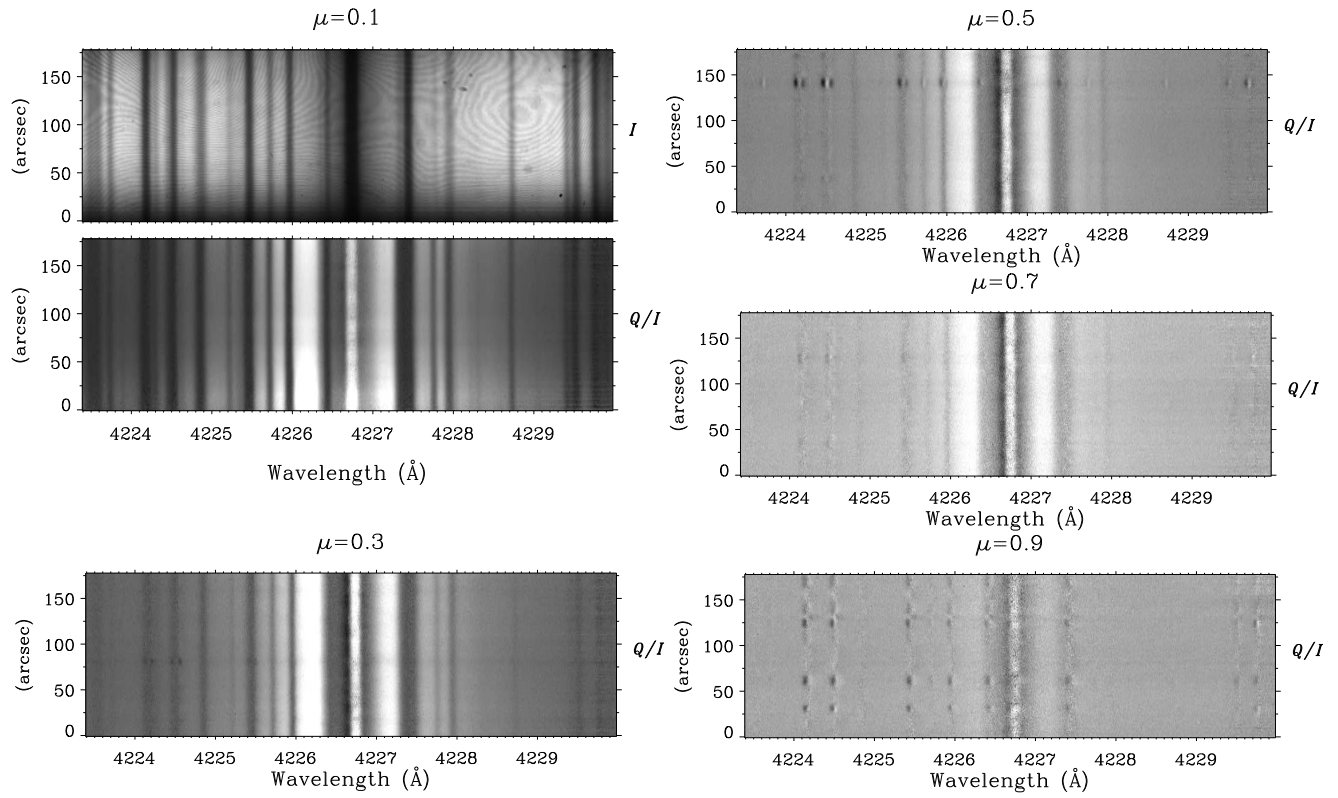


Fig. 1.— CCD images of  $I$  (only for  $\mu = 0.1$ ) and  $Q/I$  at 5 selected  $\mu$  values of the Ca I 4227 Å line. The observations were taken on October 16, 2012 at IRSOL in Switzerland.

## 2. Observational details

The CLV observations of the Ca I 4227 Å line presented in this paper were obtained with the Zurich Imaging Polarimeter-3 (ZIMPOL-3) (Ramelli et al. 2010) at IRSOL (Istituto Ricerche Solari Locarno) in Switzerland on October 16, 2012. The observations were taken at 14 different  $\mu$  positions (0.10, 0.15, 0.20, 0.25, 0.30, 0.35, 0.40, 0.45, 0.50, 0.60, 0.70, 0.80, 0.90 and 1.0) starting from the heliographic north pole at  $\mu = 0.1$  up to the disk center at  $\mu = 1$ . Figure 1 shows the CCD images of the Ca I 4227 Å line at 5 selected positions on the solar disk. The polarization modulation was done with a piezo-elastic modulator (PEM). The spectrograph slit was 60  $\mu\text{m}$  wide corresponding to a spatial extent of 0.5'' on the solar disk. The CCD covered 190'' along the slit. The CCD images have 140 effective pixel resolution elements in the spatial direction, with each element corresponding to 1.38'', and 1240 pixels in the wavelength direction, with one pixel corresponding to 5.30 mÅ.

To keep the solar image position stable, the primary image guiding system is used (Küveler et al. 2011). In addition, below  $\mu = 0.35$  a rotating glass tiltplate is used to keep under control the distance between the spectrograph slit and the solar limb image. The slit jaw image is digitized by a dedicated CCD camera. An algorithm recognizes the solar limb and the spectrograph slit position on the image. This allows the calculated desired distance between the limb and the slit to be set by automatic control of the tilt plate. Note that this plate is set after the polarization analyzer and hence does not introduce spurious polarization signatures. At each  $\mu$  position a measurement is obtained by adding 300 single frames, each of them are obtained with an exposure time of 1 sec. Therefore the effective integration time is 8 minutes. The precision of the pointing at a chosen  $\mu$  position over 8 minutes using the tiltplate is limited to about 1'', which is less than the size of one pixel.

An improvement of these measurements is related to the absolute precision which we could reach in measuring  $Q/I$ . Previously, the zero polarization value needed to be defined manually was based on indirect considerations (for example the CLV of the continuum polarization). For the data

set described in this paper we could reach an absolute precision of about  $5 \times 10^{-5}$ . This is mainly due to: a) the precise control of limb distance, allowed by the tiltplate system described above, b) the improved control of the rotation of the optical devices, including the polarization analyzer in front of the slit (to compensate for the image rotation originated by the Gregory Coudé telescope), and c) the optical compensation of the instrumental linear polarization, which is a source of variable offset effects, with an oriented glass plate set in front of the polarization analyzer. It was thus possible to subtract from every measurement done at a defined  $\mu$  position, the polarization level measured at disk center in a quiet region. For symmetry reasons the linear polarization in the continuum is expected to be zero at the disk center. In this way all residual instrumental linear polarization signatures are taken into account.

### 2.1. Stray light correction

The observed profiles contain contribution from the spectrograph stray light which is about 2 % of the continuum intensity. Here we correct both the intensity and polarization profiles for stray light. The effect of stray light, including both its intensity and polarization, was treated in Stenflo (1974). Below are the details of the procedure we have followed.

In the absence of stray light but with instrumental polarization (cross talk from  $I(\lambda)$ ), the  $I(\lambda)$  and  $Q(\lambda)$  parameters after polarization calibration are  $I'(\lambda) = I(\lambda)$  and  $Q'(\lambda) = Q(\lambda) + M_{21}I(\lambda)$ , if we assume that the Mueller matrix has been normalized ( $M_{11} = 1$ ), there is no telescope depolarization or it has been calibrated away ( $M_{22} = 1$ ), and that polarization cross talk from  $U$  and  $V$  can be disregarded.  $M_{21}$  is the spectrally flat instrumental polarization, which for convenience will be renamed as  $p_z$ , since it represents a flat offset of the zero point of the polarization scale.

In the presence of stray light with an intensity that is a fraction  $s$  of the continuum intensity  $I_c$  and has a polarization  $p_s$ , the apparent or observed Stokes parameters are

$$\begin{aligned} I_{obs}(\lambda) &= I(\lambda) + sI_c, \\ Q_{obs}(\lambda) &= Q(\lambda) + p_z(I(\lambda) + sI_c) + p_s sI_c. \end{aligned} \quad (1)$$

We now introduce the notation  $r(\lambda) = I(\lambda)/I_c$  and  $r_{obs}(\lambda) = I_{obs}(\lambda)/I_{obs,c}$  for the rest intensities. For clarity we attach a  $\lambda$  to the quantities that are spectrally structured, in contrast to the three free parameters of our problem, namely,  $s$ ,  $p_s$ , and  $p_z$ , which are constant and spectrally flat. Then

$$r(\lambda) = (1 + s)r_{obs}(\lambda) - s. \quad (2)$$

Similarly we define the intrinsic polarization  $p(\lambda) = Q(\lambda)/I(\lambda)$  and the apparent polarization  $p_{obs}(\lambda) = Q_{obs}(\lambda)/I_{obs}(\lambda)$ . One can easily show that

$$p(\lambda) = \left(1 + \frac{s}{r(\lambda)}\right)[p_{obs}(\lambda) - p_z] - \frac{s}{r(\lambda)}p_s. \quad (3)$$

To calculate  $p(\lambda)$  from the observations we need to insert the expression for  $r(\lambda)$  from Equation (2) into Equation (3).

$p_s$  represents the intrinsic polarization as averaged over the wide spectral range that contributes to the stray light. A major source of spectrograph stray light are grating ghosts that sample discrete wavelengths spread over a large wavelength range. In the absence of other information, the best estimate of  $p_s$  is probably  $p_s \approx p_c$ , i.e., to set it equal to the continuum polarization.

The determination of  $p_z$  is best made for a disk center recording that is done immediately before or after the measurement at the given  $\mu$  position (so that one can assume that the instrumental polarization has not changed). At disk center the solar scattering polarization is zero, so the apparent polarization that we see is simply  $p_z$  (in contrast to measurements of disk center, where  $p_z$  is mixed with intrinsic solar polarization).

It is important to realize that the problem of correcting for the zero point of the polarization scale is entirely decoupled from the stray light issue. It is the first step to be done, and it gives us the spectrum

$$p'(\lambda) = p_{obs}(\lambda) - p_z, \quad (4)$$

which would equal to  $p(\lambda)$  in the absence of stray light. To correct  $p'(\lambda)$  for stray light we do not need to refer to  $p_z$  or disk center observations. The way in which the stray light correction enters can be seen by rewriting Equation (3) as

$$p(\lambda) = p'(\lambda) + \frac{s}{r(\lambda)}(p'(\lambda) - p_s). \quad (5)$$

If the stray light were unpolarized, then the stray light scaling factor  $s/r(\lambda)$ , which is large where the rest intensity  $r(\lambda)$  is low, acts to amplify the polarization amplitudes  $p'(\lambda)$ . In the presence of stray light polarization, however, the scaling factor only acts on the amplitude with respect to the  $p_s$  level rather than with respect to the zero level. The stray light polarization therefore reduces the effect of the stray light correction. For polarization amplitudes that is equal to  $p_s$  (which represents a broad band polarization background that may be approximated with the continuum polarization level  $p_c$ ), the stray light correction does not have any effect at all. For the Ca I 4227 Å line, however, the core polarization is usually larger than  $p_c$ . In this particular case the stray light polarization becomes a second-order effect (since  $sp_c$  is a product of two small quantities). Parameter  $s$  is determined exclusively from fitting the Fourier Transform Spectrum (FTS) of Kurucz et al. (1984), in the same context as the spectral broadening is determined. The above considerations give us a rather well defined procedure to determine (within the framework of our idealized model) unique estimates of the parameters  $s$ ,  $p_z$ , and  $p_s$ . Using these estimates we can correct both the  $I(\lambda)$  and  $Q(\lambda)/I(\lambda)$  spectra for stray light. In other sections we have dropped the  $\lambda$  dependence of  $I$  and  $Q$  for notational simplicity.

While the observed spectra are corrected for stray light, they have not been corrected for spectral broadening, because the instrumental profile is not known with the precision that is needed to allow a deconvolution. The theoretical spectra on the other hand, which are used for comparison with the observed spectra, need to be spectrally broadened to emulate the observations. However, one should not apply stray light to the theoretical spectra, since one can easily do the correction to the observed spectra itself. In this way we keep the presentation of the theoretical results independent of the particular properties of the instrument used for the observations, with the single exception of spectral broadening.

### 3. Modeling of the CLV observations

In this section we describe the modeling procedure we have followed to model the CLV of the Ca I 4227 Å line. We started with an aim of

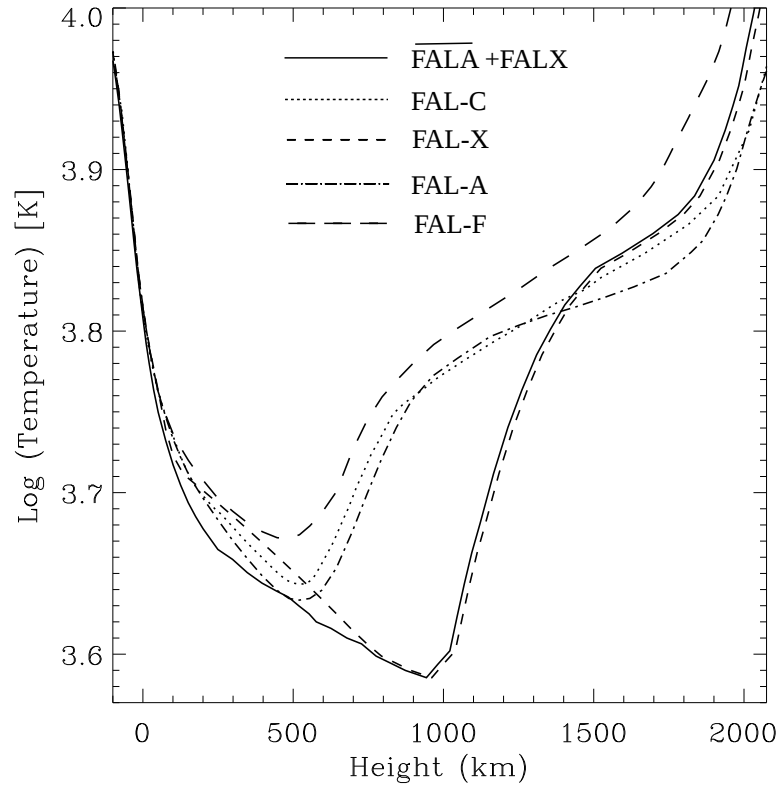


Fig. 2.— Temperature structure of four standard models FAL-A, FAL-C, FAL-F and FAL-X used in our studies. Along with these standard models the temperature structure of the new model atmosphere  $\overline{\text{FALA}} + \text{FALX}$  is also shown.

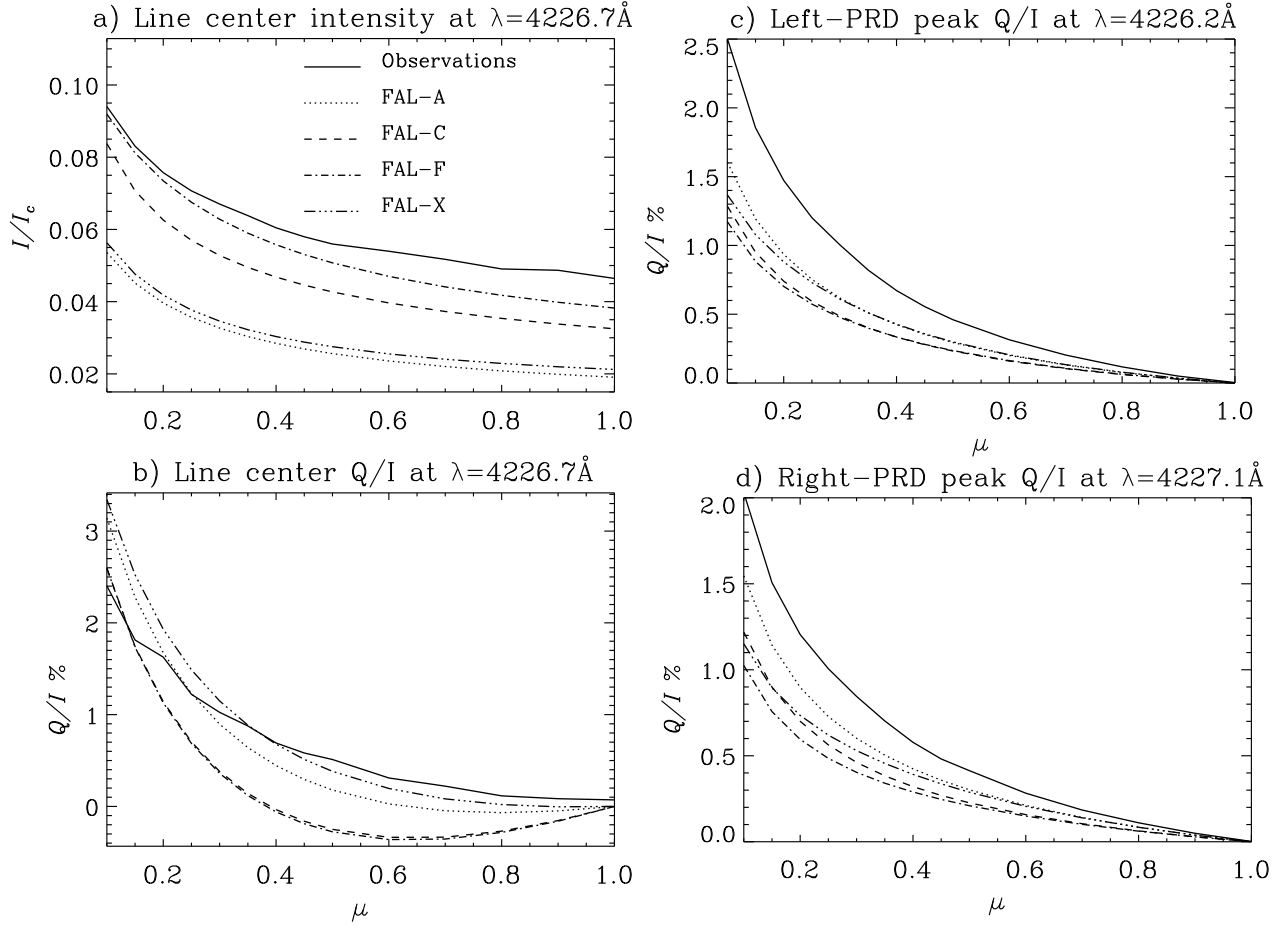


Fig. 3.— Observed (solid line) and calculated intensity and polarization signals as function of  $\mu$  (observed at 14 points) at three different wavelength positions in the line profile. The spectra are calculated for standard models FAL-X, FAL-C, FAL-A, and FAL-F.

finding a single 1-D atmosphere that can simultaneously fit ( $I$ ,  $Q/I$ ) CLV of the Ca I 4227 Å line. As a first step towards this, we begin the modeling of the observed profiles by solving the polarized RT equation for a two-level atom. The one-dimensional polarized RT equation along with the other necessary equations, in the non-magnetic regime, used in this paper are described in detail elsewhere (see Anusha et al. 2010). The elastic collision rates used in this paper are computed following the theory presented in Barklem & O'Mara (1997). Also, the modeling is done here using a two-stage process where the intensities are computed using a PRD capable MALI (Multi-level Approximate Lambda Iteration) code of Uitenbroek (2001) in the first stage. In the second stage, the polarization profiles are computed perturbatively by solving the polarized transfer equation. The details of such a two-stage modeling procedure is described in Holzreuter et al. (2005, see also Anusha et al. 2010). The atom model of the Ca I used in the present paper is same as the one discussed in Anusha et al. (2010). Hence we do not repeat the details here.

In our studies we use four standard 1-D model atmospheres of the Sun namely - FAL-A, FAL-C, FAL-F (Fontenla et al. 1993) and FAL-X (Avrett 1995). The temperature structure of these models are shown in Figure 2. Along with the standard models, the temperature structure of our newly constructed model  $\overline{\text{FALA}} + \text{FALX}$  is also shown in the figure, details of which will be discussed in Section 3.2.

### 3.1. CLV behavior at three wavelength positions

The observed  $Q/I$  profiles of the Ca I 4227 Å line show three prominent features. They are, the line center at 4226.7 Å, the blue wing PRD peak at 4226.2 Å and the red wing PRD peak at 4227.1 Å. While the line center of the Ca I 4227 Å line is formed within a height range of 700 - 1000 km (covering  $0.9 \leq \mu \leq 0.1$ ), the blue and the red wing PRD peaks are formed at a height of 150-250 km above the level where the vertical continuum optical depth at 5000 Å is unity. To get an idea of the behavior of the polarized spectra as a function of  $\mu$ , we plot the angular dependence of intensity (only at line center) and linear polarization at these chosen wavelength positions in Figure 3 com-

puted using the standard 1-D model atmospheres. As expected, it can be seen from Figure 3 that the degree of linear polarization decreases to zero towards the disk center due to symmetry in the scattering geometry.

Panels (a) and (b) of Figure 3 show a comparison of the observed and theoretical CLV of  $I$  and  $Q/I$  respectively at the line center wavelength. We see that the hottest model FAL-F (dot-dashed line) is more suited for modeling the CLV of line center intensity. But the same model is not at all good for  $Q/I$ . Instead it is the coolest model FAL-X which provides the closest fit to the observed  $Q/I$ . This contrasting behavior seems to point at the fact that we need two different temperatures to simultaneously fit  $I$  and  $Q/I$  at the line center. From Figure 3 (b) we see that the theoretical profile computed using FAL-A also falls close to the observed CLV profile of  $Q/I$ . We consider the FAL-X atmosphere rather than FAL-A to provide a better fit to the observed  $Q/I$  at the line center for the following reasons: At the line center and when  $\mu$  is small, we always expect the non-magnetic  $Q/I$  amplitude to be larger as compared with the observed  $Q/I$ , because the observed  $Q/I$  includes depolarization by magnetic fields. As we go to larger  $\mu$  the magnetic fields may enhance the core polarization amplitude. Such a behavior was noted by Faurobert-Scholl (1994), who points out that there are enhancement effects due to magnetic fields when  $\mu > 0.4$  (this will be discussed in detail in Section 3.2.1). We found the FAL-X model to better satisfy this behavior. Thus we see from Figure 3 (b) that the theoretical values of  $Q/I$  at line center when computed with FAL-X are larger than the observed  $Q/I$  for  $\mu < 0.4$ , while FAL-A shows this behavior only for  $\mu < 0.25$ . Besides this, the theoretical  $Q/I$  computed with FAL-A falls much below the observed  $Q/I$  as we move towards larger values of  $\mu$ . For these reasons we consider FAL-X to give a consistent overall fit to the observed CLV of  $Q/I$  at line center, while FAL-A does not.

On the other hand, Figures 3 (c) and (d) show the CLV profiles of  $Q/I$  at the blue and red wing PRD peak wavelength positions respectively. We notice that both FAL-F and FAL-X model atmospheres fail to provide a fit to the PRD peaks. It is the theoretical CLV profiles from the FAL-A model that falls closest to the observed CLV of



$Q/I$ . Thus we do not find a single 1-D atmospheric model which can provide a fit to the entire Stokes ( $I$ ,  $Q/I$ ) profiles simultaneously. As a next step we explore the possibility of obtaining a fit to the CLV of the Stokes profiles through small modification of the temperature structure at appropriate heights, of the original FAL models.

### 3.2. Theoretical fit to the CLV of $Q/I$ profiles

From Figures 3 (c) and (d) we see that though the theoretical profiles from the model FAL-A falls closest to the observed CLV of  $Q/I$ , it fails to provide a satisfactory fit to the  $Q/I$  observations. In order to obtain a better fit to the observed CLV of  $Q/I$  profiles, we adopt modification of temperature structure at the heights where PRD peaks are formed. We focus our attention only on fit to the  $Q/I$  profiles. Since FAL-A model atmosphere provides closest fit to the observed  $Q/I$  profiles, we choose this model for further modifications. Accordingly, the temperature of the FAL-A standard model at these heights is reduced by about 200 K. This newly constructed model is denoted as  $\overline{\text{FALA}}$ . This new model provides a better fit to the wing PRD peaks at all the limb distances.

After achieving a fit to the PRD peaks, we concentrate on obtaining a fit to the linear polarization at the line center. From Figure 3 (b) we see that it is the FAL-X model atmosphere which fits the observed profiles, the closest. Thus, to obtain a satisfactory fit to the entire  $Q/I$  profile we need to combine these two model atmospheres ( $\overline{\text{FALA}}$  and FAL-X) at appropriate heights. The two models are combined such that the new model atmosphere has the temperature structure of  $\overline{\text{FALA}}$  up to a height of 400 km, and the temperature structure of FAL-X in the heights above 400 km. The temperature structure of the new combined model atmosphere ( $\overline{\text{FALA}} + \text{FALX}$ ) is shown as the solid line in Figure 2. The results obtained using this combined model atmosphere are discussed below.

#### 3.2.1. Results from the new combined model atmosphere

The theoretical profiles obtained using  $\overline{\text{FALA}} + \text{FALX}$  model atmosphere are shown in Figure 4 (dotted line). Also a comparison between the observed and theoretical  $Q/I$  CLV curves at the blue

and red wing PRD peaks and at the line center wavelength using the combined model is shown in Figure 5 (dotted line). These theoretical profiles show that we obtain an overall satisfactory fit to the  $Q/I$  profiles at all the  $\mu$  positions using the combined model atmosphere. The theoretical profiles computed using the combined model atmosphere in Figures 4 and 5 include suitable spectral smearing. This is done by convolving the theoretical spectra with a Gaussian profile having a FWHM of 50 mÅ. The smearing accounts for both the instrumental broadening (40 mÅ) and the broadening by macro-turbulent velocity fields (30 mÅ). The macro-turbulent smearing corresponds to a velocity of 1.28 km/s. For the deep lines like the Ca I 4227 Å, the effects of the stray light corrections (the stray light correction procedure is described in Section 2.1) are much more important than the smearing. The intensity ( $I$ ) profiles from the combined model seem to fit the observed data at all the  $\mu$  positions, with the exception of the line core, where we fail to get a satisfactory fit. At the formation heights of the line center, a rest intensity fit requires a hotter atmospheric model like the FAL-F which is not suitable for achieving a good fit to the  $Q/I$  profile - which indeed requires cooler models like the FAL-X. In spite of the carefully determined stray light correction (by  $s = 2\%$ ) to the observed Stokes  $I$  profiles, the central line depth still does not come close to reproduce the very deep theoretical  $I$  profiles. We have also carried out tests with the use of different micro- and macro-turbulent velocities, and we found that the choice of turbulent velocity does not significantly affect the rest intensity of the Stokes  $I$  profiles.

From Figures 4 and 5 we notice that for  $\mu \leq 0.35$  the observed line center  $Q/I$  is less than the theoretical value and for  $\mu > 0.35$  it is greater than the  $Q/I$  predicted theoretically. Such a discrepancy was also encountered by Faurobert-Scholl (1994) while modeling the CLV of the line center  $Q/I$  of the Ca I 4227 Å line. The author found that the ratio of  $(Q/I)_{\text{obs}}$  and  $(Q/I)_{\text{theory}}$  at the line center was close to unity for smaller  $\mu$  values ( $\mu < 0.4$ ) and much greater than one for larger  $\mu$  values. However her treatment did not include the stray light corrections. We recall that the observed profiles in Figure 5 are corrected for the stray light. In Faurobert-Scholl (1994) though an

explanation of the physical mechanism behind this enhancement in polarization for larger  $\mu$  values was anticipated based on accelerated motions in the chromosphere, but it was not completely justified.

To examine this discrepancy further, we plot the variation exhibited by  $Q/I$  along the spectrograph slit at the line center (solid line) and compare it with the  $Q/I$  in the blue wings (dotted line) in Figure 6. The observed line center  $Q/I$  values are smoothed over a rectangular box corresponding to  $5''$  to reduce contribution from noise. These smoothed values of the observed  $Q/I$  at the line center are used for all further computations. From Figure 6 we see that the  $Q/I$  at the line center shows more variation along the slit than at the blue wing peak. This indicates the presence of varying horizontal magnetic fields and their possible role in modifying the line center  $Q/I$ . These varying magnetic fields can in turn be used to understand the observed line center  $Q/I$  which are greater than the theoretically predicted values. One possible explanation for this discrepancy could be that observed line center  $Q/I$  for  $\mu > 0.35$  is enhanced due to the Hanle effect by these varying fields (see also Faurobert-Scholl 1994). This enhancement is very prominent in case of the near disk center observations (see Anusha et al. 2011). However, in our case, it sets in for  $\mu > 0.35$  and increases as  $\mu \rightarrow 1$ . This is a clear evidence for highly structured, resolved, oriented magnetic fields (predominantly horizontal) in the solar atmosphere. However the dotted line in Figure 6 (for the blue wing) do not exhibit the type of spatial fluctuations that is seen for the line center (solid line). This is because the Hanle effect is absent in the wings. We also note that the spatial variation close to the limb in the blue wing is not really spectrally flat. The details regarding this will be discussed in Section 4.

### 3.2.2. *The impact of temperature structure modifications on the standard model atmospheres*

In the previous section we described the necessity of constructing a new model in order to obtain a fit to the CLV of the Stokes profiles. To this end, a new model was constructed by combining two standard models after modifying their temperature structures at the desired heights. The

new combined model thus constructed will provide a fit to the CLV of the observed  $Q/I$ . The physical consistency of the newly constructed atmospheric model with the modified temperature structure has been checked by verifying that it satisfies hydrostatic equilibrium at all heights.

Next we examine the fit to the CLV of the continuum intensity over a wavelength range spanning from the visible to the infrared. The theoretical continuum intensity obtained using the new model should fit the observed data at all the limb distances and for a range of wavelengths. Figure 7 shows the limb darkening function computed using the standard models and our new model atmosphere  $\overline{\text{FALA}} + \text{FALX}$  for a range of wavelengths and  $\mu$  values. The theoretical values from different models are compared with the observed data from Neckel & Labs (1994). The dash-triple-dotted line represents the theoretical values from the new model  $\overline{\text{FALA}} + \text{FALX}$ . We see that the best fit to the observations is provided by the FAL-C model. The combined model though is successful in providing a CLV fit to the observed  $Q/I$  and satisfies the equilibrium conditions, it does not provide the best fit to the observed CLV of the limb-darkening function and to the observed CLV intensity.

This leads us to the conclusion that it is indeed not possible to obtain a simultaneous fit to all the various types of data with a single 1-D model atmosphere. One needs a different atmosphere for each observable. In search of a single model which satisfies all the observational constraints, the next obvious step would be to use the two-component modeling approach with appropriate mixing ratios as done in Holzreuter & Stenflo (2007). In the section below we discuss why we cannot adopt such a procedure in modeling the CLV of the Ca I 4227 Å line.

### 3.2.3. *The two-component modeling approach*

In modeling the CLV observations of the Ca II K line, Holzreuter & Stenflo (2007) explored the possibility of constructing a two-component model atmosphere. This was constructed by mixing the results obtained from two standard model atmospheres in appropriate ratios. Such a method was adopted by making CLV plots of the Ca II K line as shown in their Figure 1. As seen from their figure, the original models FAL-X and FAL-C produce theoretical CLV curves which fall respec-

tively above and below the observed CLV curve of  $Q/I$ . Hence they combine results from these two standard models with appropriate mixing ratios to achieve the required fit. In Figure 3 of the present paper we make similar plots of the CLV for the Ca I 4227 Å line. As seen from Figure 3, none of the standard model atmospheres produce a theoretical CLV curve which falls above the observed CLV curve. This does not allow us to apply the same kind of two-component modeling procedure as described by Holzreuter & Stenflo (2007). This suggests that we need to go beyond 1-D modeling in the direction of 2-D or 3-D modeling to obtain a simultaneous fit to the  $(I, Q/I)$  at all the limb distances. Such efforts are beyond the scope of this paper. However 1-D models with modified temperature structures serve as a good initial step to such elaborate computations. The failure of 1-D modeling approach does not preclude the use of a given line profile for purposes like magnetic field determination. To demonstrate this fact, in the next section, we perform observational analysis of the Ca I 4227 Å line to determine the field strengths for smaller  $\mu$ .

#### 4. Determination of the field strength

In the present section we use an approach similar to that of Bianda et al. (1998, 1999) to determine the field strength at different limb distances. Since the observed  $Q/I$  is influenced by so many factors besides the magnetic field, it is imperative to apply *differential* techniques to isolate the Hanle effect from the multitude of other effects. This can be done by using the wing polarization as a reference, since it has been well established that the Hanle effect only operates in the line core but is absent in the wings.

If we in Figure 6 compare  $Q/I$  in the line core (solid lines) and in the blue wing (dotted lines), we notice that the line core exhibits large spatial variations along the slit, in contrast to the blue wing. Nevertheless, the blue wing polarization exhibits large-scale slow drifts along the slit, which increase significantly as we approach the limb. Much of this can be explained in terms of a geometric effect due to the limb curvature. Since the solar limb is curved while the slit is straight, the limb distance (or  $\mu$ ) will vary along the slit. This effect will increase in significance as we get closer to the

limb. It is an effect that is nearly identical for the line core and wing (since the core and wing have nearly the same relative center-to-limb variations) and therefore can be eliminated when forming the core to wing ratio. Similarly, any other unidentified instrumental effect would ratio out. In principle there may also be non-magnetic effects of solar origin, like spatial variations of the radiation-field anisotropy, which may be different between core and wings and therefore would not fully ratio out (although they should be suppressed when forming the ratio, since the non-magnetic fluctuations in the core and wings are not uncorrelated). However, with our rather low spatial resolution and long integration times, these solar effects are expected to be miniscule.

We therefore have strong reasons to believe that practically all the spatial fluctuations that we see in the  $Q/I$  core to wing ratio is exclusively due to magnetic fields via the Hanle effect. Instead of directly using this ratio as our differential measure, we can scale it with the slit average of the wing polarization, to express it in polarization units. This scaling is equivalent to the assumption that the wing polarization should be spatially flat after all effects of limb curvature, unidentified instrumental effects, and solar non-magnetic effects have been corrected for. We thus correct the line core polarization amplitude with the following relation

$$(Q/I)_{corrected}^{line\ center} = \frac{(Q/I)_{uncorrected}^{line\ center}}{P_b} < P_b >, \quad (6)$$

where  $P_b = (Q/I)^{blue\ wing\ peak}$  for each pixel and  $< P_b >$  is the spatial average of  $P_b$  along the slit. With this correction we plot in Figure 8 the CLV of the spatially averaged  $Q/I$  at the blue wing and the corrected  $Q/I$  at the line center. Each “plus” symbol in bottom panel of Figure 8 represents the value of  $Q/I$  at each pixel corresponding to the line center. We notice large spatial variations along the slit in the corrected  $Q/I$  line-center data. This effect is exclusively due to the magnetic fields via the Hanle effect. In order to find the field strengths that contribute to such spatial variation, we follow the method used in Bianda et al. (1998, 1999). We would like to note that in both these papers, for the data analysis, the authors use observations taken at different periods. However in our analysis we consider only one single set of observations and the variation of  $Q/I$  along the slit

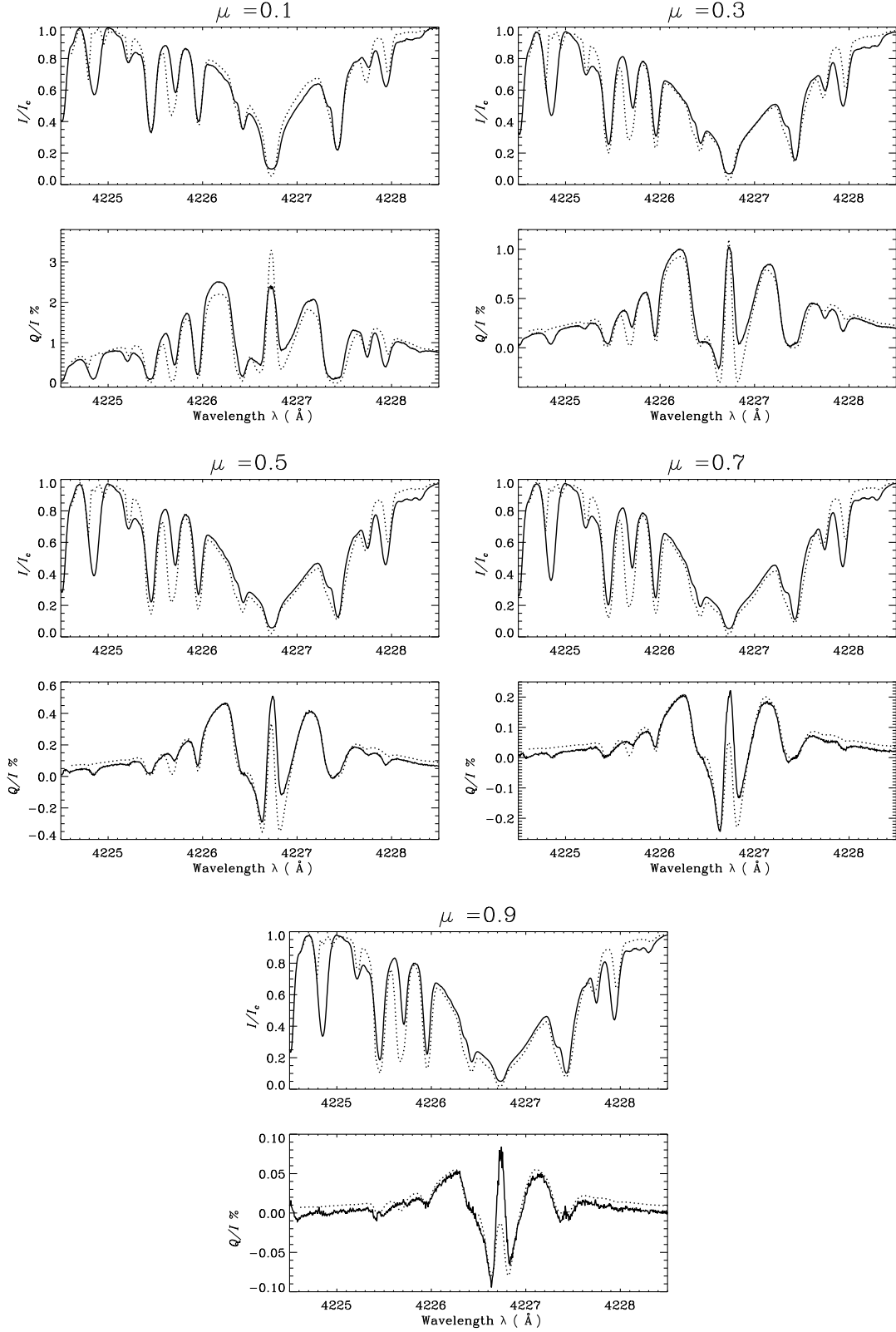


Fig. 4.— Comparison between the observed (solid line) and the theoretical (dotted line) Stokes profiles ( $I$ ,  $Q/I$ ) at different limb distances. The combined model atmosphere FALA + FALX is used to compute the theoretical profiles.

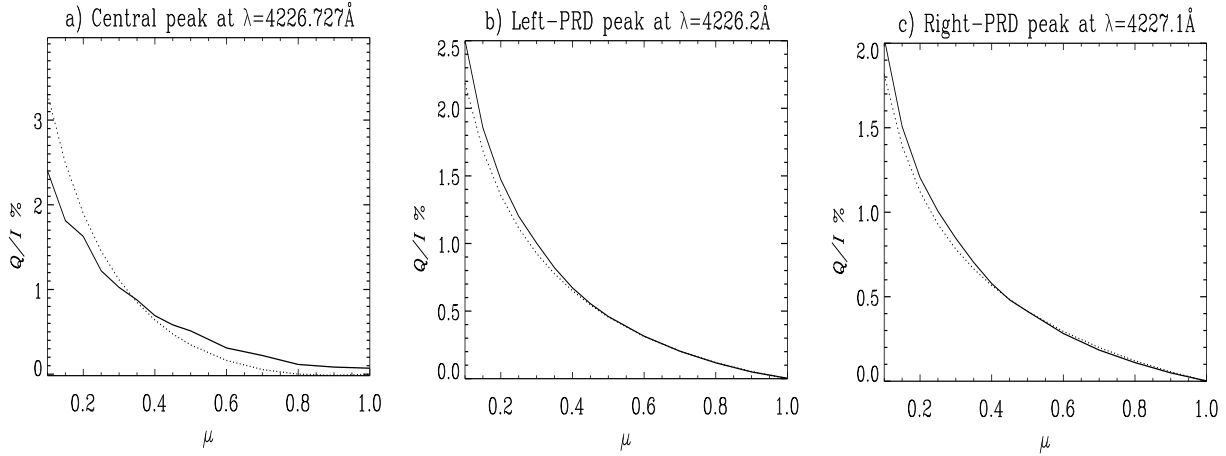


Fig. 5.— Center to limb variation of linear polarization at three chosen wavelength positions. The model atmosphere used to obtain the theoretical profiles (dotted line) is the new combined model FALA + FALX.

in these observations. To this end we construct the envelopes (continuous lines in Figure 8) to our data set, using the analytical relation

$$\frac{Q}{I} = \frac{a(1 - \mu^2)}{\mu + b}. \quad (7)$$

This relation was first introduced by Stenflo et al. (1997) where  $a$  and  $b$  are the best fit free parameters. For our studies we have chosen the same set of free parameters as given in Bianda et al. (1998, 1999). From top panel of Figure 8 we see that the dashed line ( $a = 0.33\%$ ,  $b = 0.02$ ) gives a good fit to the spatially averaged observed CLV profile in the blue wing. In the bottom panel of Figure 8 we use three different set of free parameters  $a$  and  $b$  to construct envelopes for the line center data. The envelopes constructed using the analytical relation given in Equation (7) represent the ‘non-magnetic value’ and all the values lying below this envelope are considered as the depolarized  $Q/I$  values due to the Hanle effect. From our modeling efforts we know that the magnetic fields cause an enhancement in the polarization value for  $\mu > 0.35$  (also see Faurobert-Scholl 1994). Hence this envelope fitting method is good for  $\mu \leq 0.35$  and becomes questionable for  $\mu$  larger than about 0.35. However the transition between the large angle scattering and small angle scattering is gradual and smooth. For large  $\mu$  we gradually enter into the regime of forward-scattering Hanle effect, for which the kind of techniques developed by Anusha et al. (2011) have to be adopted to

derive the field strengths. Full radiative transfer modeling is naturally needed for intermediate  $\mu$  values. Only for smaller  $\mu$  values it is possible to use a method that avoids the need for radiative transfer. In this approach, we first extract an observed depolarization factor via the envelope method and then convert this depolarization into field strength.

Thus we first determine the ratio between the line center  $Q/I$  and the corresponding envelope value. This ratio represents the depolarization factor caused by the Hanle effect for each pixel. The conversion of this factor into field strength is dependent on the choice of the envelope, since it represents a single observable, while the magnetic field vector is characterized by three parameters (its spatial components). The magnetic field is therefore underdetermined, so a conversion cannot be unique, but it is still meaningful in a statistical sense, as explained in the following.

For photospheric spectral lines an interpretational model with a spatially averaged micro-turbulent field distribution could be used to convert Hanle depolarization into field strength (Stenflo 1982, 1994), because the absence of  $U/I$  polarization in combination with insignificant spatial variations (at resolved scales) in  $Q/I$  made such a micro-turbulent interpretational model unavoidable (see also Stenflo 2013). The situation is however entirely different for strong chromospheric lines like the Ca I 4227 Å line, which al-

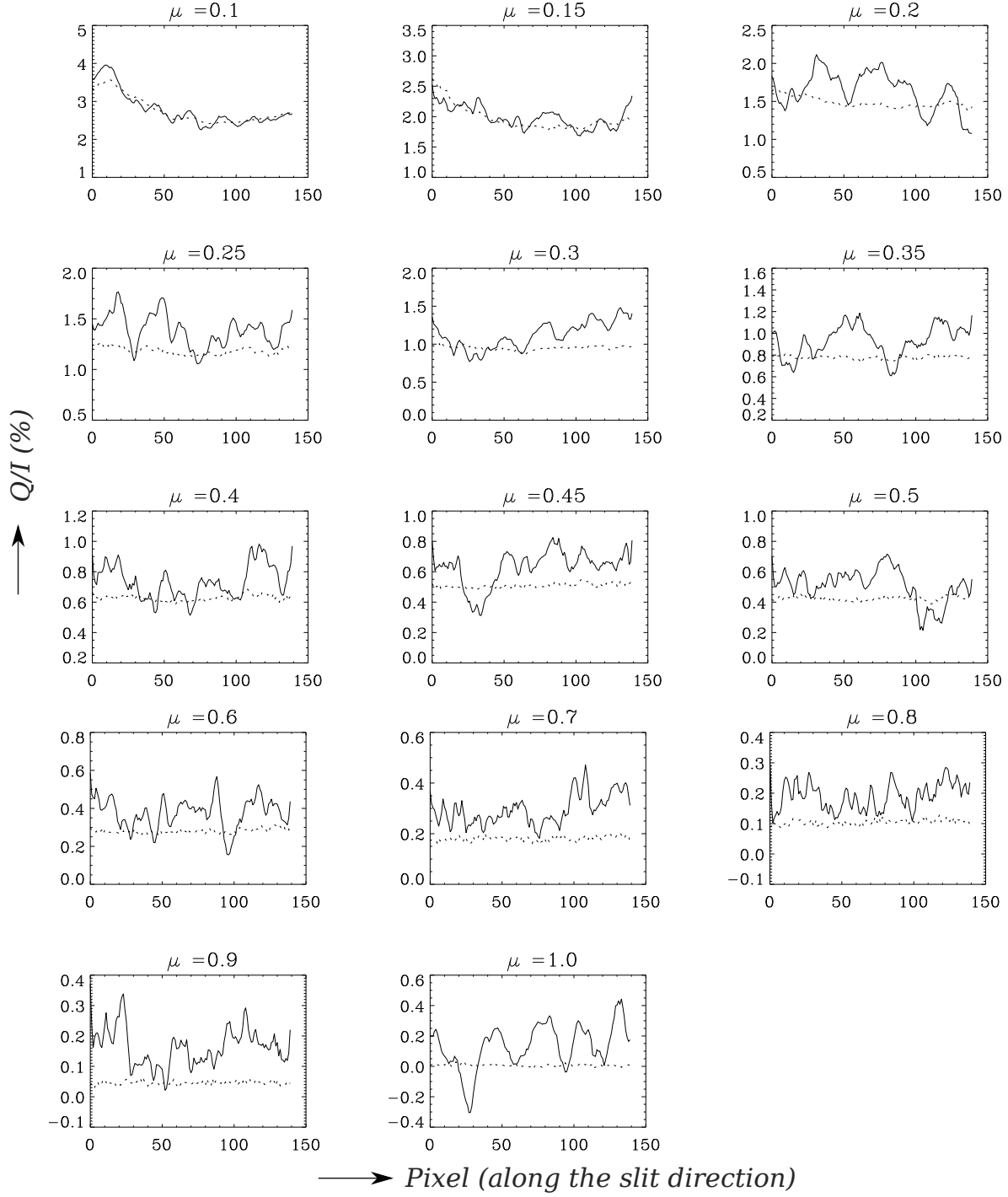


Fig. 6.— Variation of  $Q/I$  values along the slit for each  $\mu$  position (marked over the plots). The solid and the dotted lines correspond to the  $Q/I$  value at the line center and at the blue wing peak respectively.

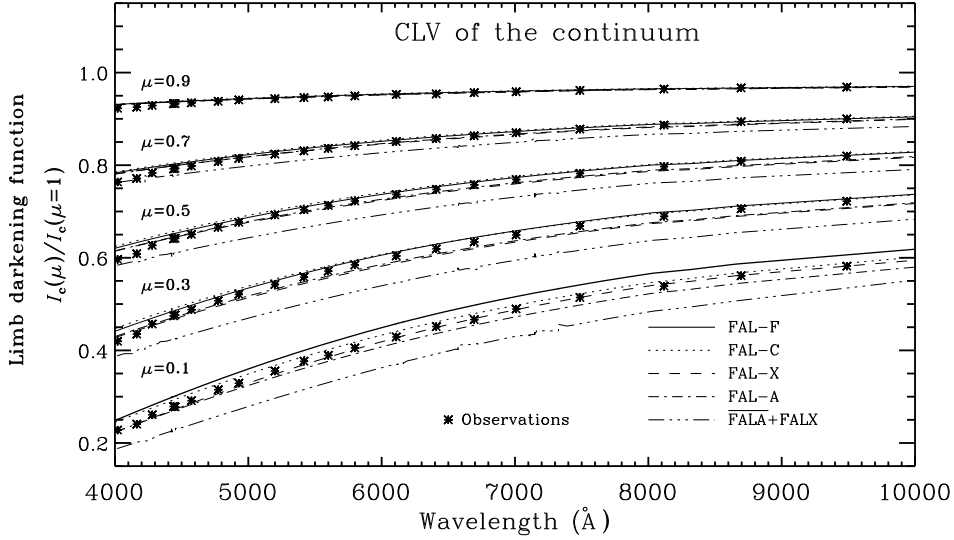


Fig. 7.— Comparison between the observed data for the CLV of continuum intensity from Neckel & Labs (1994) for a range of wavelengths and the theoretical values from different model atmospheres including FALA + FALX.

ways exhibits large spatial line-core variations in both  $Q/I$  and  $U/I$ , like those in Figure 6. As we have spatially resolved these variations, they should ideally be interpreted in terms of resolved, oriented fields rather than angular distributions. However, since the field vector is underdetermined by the single depolarization factor, we need to eliminate the ambiguity by using the statistical approach, dealing with each depolarization factor as if it were obtained through averaging over an ensemble of field elements. This approach will give field strength values that are meaningful as averages in a statistical sense.

Vertical fields are immune to the Hanle effect, depolarization can only occur if the field has a substantial inclination with respect to the vertical direction. Horizontal fields give the largest depolarization. If we assume the fields to be horizontal, but with orientations that are random in azimuth angle, and let the Hanle depolarization be determined by an ensemble average over such a field distribution, then the field strengths that we extract from this model can be considered to represent *lower limits* to the true average field strength (since there may exist less inclined fields that are less “visible” to the Hanle effect).

Chromospheric fields are expected to be largely horizontal, forming a “canopy” over the underly-

ing photosphere. The Hanle depolarization factor  $k_H$  for a horizontal field distribution with random azimuths can be written as (Stenflo 1982, 1994)

$$k_H = 1 - 0.75 \sin^2 \alpha_2, \quad (8)$$

where the Hanle mixing angle  $\alpha_K$  is given by

$$\tan \alpha_K = \frac{KB}{B_0/k_c^{(K)}}. \quad (9)$$

$B$  is the field strength to be determined,  $K = 1$  or  $2$ ,  $k_c^{(K)}$  is the collisional branching ratio for the  $2K$ -multipole and  $B_0$  is the characteristic field strength for the Hanle effect.

Figure 9 shows the histograms of the field strengths obtained when using Eqs. (8) and (9) for all pixels along the spatial direction. By definition, a depolarization factor should be less than or equal to unity, otherwise it is unphysical. However, some points give an unphysical depolarization factor, both because there is scatter of the  $Q/I$  values due to measurement noise, and because the chosen envelope may be too low. In such cases the field strength used for the histograms in Figure 9 is set to zero. The number of such zero field points depends on the choice of envelope and increases as we move away from the limb because

of the increasing contribution from the forward-scattering Hanle effect.

Figure 9 shows how the field-strength fluctuations along the slit vary with different limb distance. For the derivation of the CLV of the average field strength, which is shown in Figure 10, we do not average the field-strength histograms of Figure 9, because they are affected by measurement noise in a non-linear way (including the truncation used for the unphysical values), but we instead average the measured  $Q/I$  along the slit (causing the Gaussian instrumental noise to get greatly suppressed), and then convert the average  $Q/I$  to field strength. Since the height of line formation increases with decreasing  $\mu$ , the  $\mu$  variation displayed by Figure 10 may be interpreted in terms of a height variation of the field. In view of the limited statistical sample and the crudeness of the interpretational model the minor variations with  $\mu$  in Figure 10, which are similar to the ones obtained by Bianda et al. (1998, 1999), are not significant but are compatible with approximate constancy of the average field strength over the height range covered by our  $\mu$  range.

Note that we have limited the  $\mu$  range in Figure 10 to 0.1 - 0.35, because as mentioned before the envelope method is not applicable for larger  $\mu$  values. Note also how the derived mean field strength depends on the choice of envelope. In spite of these uncertainties, the values are generally limited to the range 6 - 10 G. We cannot choose envelopes significantly lower than the one represented by the solid line (in the bottom panel of Figure 6), because one would then get an excessive number of unphysical depolarization factors. Therefore the 6 G value can be seen as representing a kind of lower limit for the average field strength.

## 5. Conclusions

To understand the depth dependence of various physical quantities in the Sun, like the magnetic fields, it is important to model the CLV observations of suitable atomic and molecular lines. In this paper we have attempted to model such CLV observations of the well known Ca I 4227 Å line. In our approach we take into account the effects of partial frequency redistribution (PRD) and radiative transfer. The observations of this line were carried out in quiet regions on the Sun at 14 po-

sitions starting from the limb up to the disk center on October 16, 2012 at IRSOL in Switzerland. This line has the largest degree of linear polarization in the visible region of the Second Solar Spectrum and can be modeled by considering a simple two-level atom picture. When trying to model this CLV data we find that none of the standard atmospheric models, attempted by us, like the FAL-F, FAL-A, FAL-C, and FAL-X could simultaneously fit the observed  $(I, Q/I)$  profiles at all the limb distances. To model the CLV of the line center intensity we need FAL-F model which is the hottest and to model the CLV of the linear polarization at line center we need the coolest model FAL-X. In order to obtain a fit to the observed Stokes profiles, modifications in the temperature structure of the standard models become necessary. With suitable modifications in the desired height range, we constructed  $\overline{\text{FALA}}$  and later combined it with FAL-X. While the  $\overline{\text{FALA}}$  model gives a good fit to the PRD peaks, the FAL-X gives a good fit to the line center. The combined model has the temperature structure of  $\overline{\text{FALA}}$  up to 400 km, and that of FAL-X in the upper layers. This new combined model atmosphere gives a good fit to the entire  $Q/I$  at all values of  $\mu$ . Also in modeling efforts we found that the Hanle effect not only depolarizes the line core of  $Q/I$  (which is true for smaller  $\mu$ 's) but also enhances the line core  $Q/I$  for larger  $\mu$  values. This might be due to the highly structured horizontal magnetic fields in the solar atmosphere.

Though the new combined model provides a fit to the CLV of the observed  $Q/I$ , it fails to reproduce the observed CLV of the continuum limb-darkening function and the CLV of the observed line core intensity. This failure of 1-D models in order to simultaneously fit the observed  $(I, Q/I)$  CLV profiles do not restrain the use of the Ca I 4227 Å as a tool to map the magnetic fields. To support this claim, we carried out observational analysis to determine field strength using the Ca I 4227 Å for smaller  $\mu$  values.

To conclude, it appears that no single 1-D atmosphere can completely provide a good representation of the actual solar atmosphere. This shows that the solar atmosphere has a far more complex structure. To simultaneously satisfy the various observational constraints it is therefore unavoidable to go beyond such 1-D models - a difficult problem that needs to be approached step



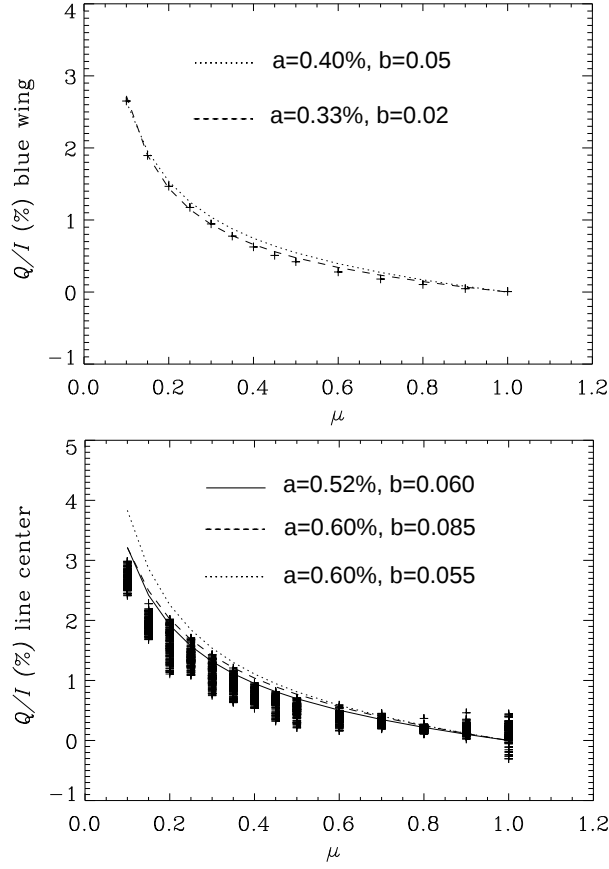


Fig. 8.— CLV of  $Q/I$  at the blue wing PRD peak (top panel) and at the line center (bottom panel). Plus sign represents the  $Q/I$  value at each pixel along the slit in the bottom panel and spatially averaged value of  $Q/I$  in the top panel. The solid, dotted and dashed curves are obtained using the empirical relation given in Equation (7). The corresponding value of the free parameters  $a$  and  $b$  are indicated in the figure.

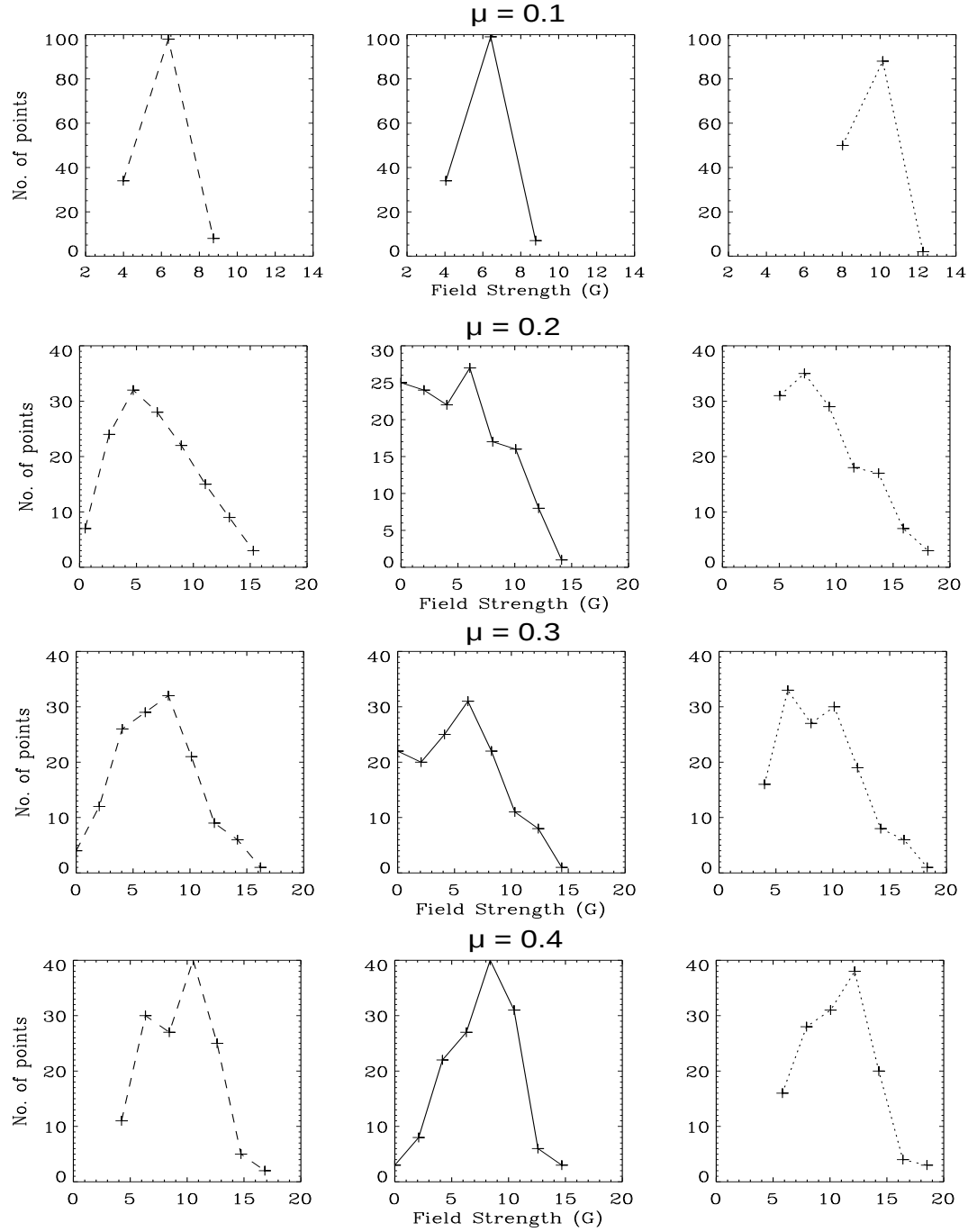


Fig. 9.— Histogram of the field strength at different  $\mu$  positions. Field strengths are computed for each depolarization value in the spatial direction. Different panels along the row for each  $\mu$  correspond to field strengths obtained using different envelopes. The solid, dotted and dashed lines respectively correspond to the solid, dotted and dashed envelopes in Figure 8.

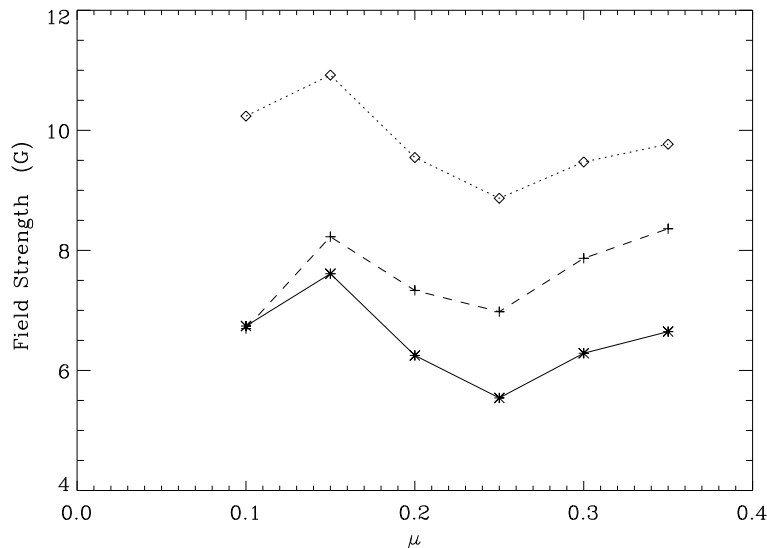


Fig. 10.— Mean value of field strength (G) derived from averaged  $Q/I$  value along the slit. The solid, dotted and dashed lines correspond to the mean field strength derived from the corresponding envelopes indicated in Figure 8.

by step. This conclusion is not at all a technical failure meaning that our inability to obtain a simultaneous perfect fit to the CLV of the  $(I, Q/I)$  has nothing to do with the weakness of our approach or the method followed in using 1-D solar atmospheres. Instead it is a “profound failure” indicating that the atmosphere of the Sun has such a complexity that it is not possible to represent it in terms of a single 1-D atmosphere. It could mean that the use of 1-D models for interpretations of the Second Solar Spectrum may give results that are physically incorrect (since they do not represent solar conditions), although the results may formally be mathematically correct. However, 1-D modeling efforts may still provide a guideline to the more systematic and sophisticated modeling efforts.

We are grateful to Dr. Han Uitenbroek for providing us with his realistic atmospheric modeling code. Research at IRSOL is financially supported by State Secretariat for Education, Research and Innovation, SERI, Canton Ticino, the city of Locarno, the local municipalities, the Foundation Aldo e Cele Daccò and the Swiss National Science Foundation grant 200021-138016. RR acknowledges financial support by the Carlo e Albina

Cavargna foundation. We are grateful to the referee for very detailed and useful comments which helped in improving the paper substantially.

## REFERENCES

- Anusha, L. S., Nagendra, K., N., Stenflo, J. O., Bianda, M., Sampoorana, M., Frisch, H., Holzreuter, R., & Ramelli, R., 2010, *ApJ*, 718, 988
- Anusha, L. S., Nagendra, K., N., Bianda, M., Stenflo, J. O., Holzreuter, R., Sampoorana, M., Frisch, H., Ramelli, R., & Smitha, H., N., 2011, *ApJ*, 737, 95
- Auer, L. H., Rees, D. E., & Stenflo, J. O. 1980, *A&A*, 88,302
- Avrett, E. H. 1995, in *Infrared tools for Solar Astrophysics: What’s Next?* ed. J. R. Kuhn, & M. J. Penn (Singapore: World Scientific), 303
- Barklem, P. S., & O’Mara, B. J. 1997, *MNRAS*, 290, 102
- Bianda, M., Solanki, S. K., & Stenflo, J. O., 1998, *A&A*, 331, 760

- Bianda, M., Stenflo, J. O.; Solanki, S. K., 1999, A&A, 350, 1060
- Bianda, M., Stenflo, J. O., Gandorfer, A., & Gisler, D., 2003, in ASP conf. Ser., 286, Current Theoretical Models and Future High Resolution Solar Observations: Preparing for ATST, ed A. A. Pevtsov & H. Uitenbroek (San Francisco, CA: ASP), 61
- Bianda, M., Ramelli, R., Anusha, L. S., Stenflo, J. O., Nagendra, K. N., Holzreuter, R., Sampoorana, M., Frisch, H., Smitha, H. N., 2011, A&A, 530, L13
- Faurobert-Scholl, M., 1992, A&A, 258, 521
- Faurobert-Scholl, M., 1994, A&A, 285, 655
- Fontela, J. M., Avrett, E. H., & Loeser, R., 1993, ApJ, 406, 319
- Gandorfer, A., 2002, The Second Solar Spectrum, Vol. II, 3910 to 4630 line. VdF Hochschulverlag, Zurich
- Holzreuter, R., Fluri, D. M., & Stenflo, J. O. 2005, A&A, 434, 713
- Holzreuter, R. & Stenflo, J. O., 2007, A&A, 467, 695
- Kurucz, R. L., Furenlid, I., Brault, J. & Testerman, L, 1984, in Solar flux atlas from 296 to 1300 nm. Nat. Solar Obs. (New Mexico: Sunspot)
- Küveler, G., Dao, V. D., & Ramelli, R., 2011, AN, 332, 502
- Neckel, H., & Labs, D., 1994, Sol. Phys., 153, 91
- Ramelli, R., Balemi, S., Bianda, M., Defilippis, I., Gamma, L., Hagenbuch, S., Rogantini, M., Steiner, P., & Stenflo, J. O., 2010, in Proc. SPIE 7735, ed. I. S. McLean, S. K. Ramsay, & H. Takami, 66
- Sampoorna, M., Stenflo, J. O., Nagendra, K., N., Bianda, M., Ramelli, R., & Anusha, L. S., 2009, ApJ, 699, 1650
- Shapiro, A. I., Fluri, D. M., Berdyugina, S. V., Bianda, M., & Ramelli, R., 2011, A&A, 529, 139
- Smitha, H. N., Nagendra, K., N., Stenflo, J. O., Bianda, M., Sampoorana, M., & Anusha, L. S., 2012, A&A, 541, 24
- Smitha, H. N., Nagendra, K., N., Stenflo, J. O., & Sampoorana, M., 2013, ApJ, 768, 163
- Stenflo, J. O., 1974, Sol. Phys., 37, 31
- Stenflo, J. O., Baur, T. G., & Elmore, D. F., 1980, A&A, 84, 60
- Stenflo, J. O., 1982, Sol. Phys., 80, 209
- Stenflo, J. O. 1994, Solar Magnetic Fields: *Polarized Radiation Diagnostics* (Dordrecht: Kluwer)
- Stenflo, J. O., Bianda, M., Keller, C. U., & Solanki, S. K., 1997, A&A, 322, 985
- Stenflo, J. O., 2013, A&A Rev., 21, 66
- Uitenbroek, H. 2001, ApJ, 557, 389